We are IntechOpen, the world's leading publisher of Open Access books Built by scientists, for scientists

4,800
Open access books available

122,000
International authors and editors

135M
Downloads

Our authors are among the

154
Countries delivered to

TOP 1%
most cited scientists

12.2%
Contributors from top 500 universities

WEB OF SCIENCE™

Selection of our books indexed in the Book Citation Index in Web of Science™ Core Collection (BKCI)

Interested in publishing with us?
Contact book.department@intechopen.com

Numbers displayed above are based on latest data collected.
For more information visit www.intechopen.com

12

The Benefits of IVUS Dynamics for Retrieving Stable Models of Arteries

Aura Hernàndez-Sabaté and Debora Gil
Computer Science Dept. and Computer Vision Center, Universitat Autònoma de Barcelona
Bellaterra, Spain

1. Introduction

Artery diseases are mainly caused by the accumulation of plaque (made up of a combination of blood, cholesterol, fat and cells) inside arterial walls (Fuster, 1994). Such plaque accumulation narrows the artery blood flow (stenosis) and makes arteries inflaming and being less flexible (atherosclerosis). Artery blood flow reduction is measured by the percentage of obstruction in vessel sections and is a usual measurement previous to decide which is the best treatment (either surgical or pharmacological) for an atherosclerotic lesion. Depending on the histological composition of the plaque, its (bio-mechanical) physical behavior will be different, making it more or less unstable (vulnerable plaques) and, thus, resulting in a different risk for the patient (Kakadiaris et al., 2006). Early detection of plaque composition is a main step for planning the most suitable treatment (angioplasty, stent apposition, ...) and might prevent further thrombosis potentially leading to a fatal heart attack. Tissue bio-mechanical properties play an important role in the diagnosis and treatment of cardiovascular diseases. The main mechanical properties currently under study are radial strain, which is related to plaque type and vulnerability (Céspedes et al., 2000), and shear stress, which influences the probability of plaque accumulation (Wentzel et al., 2001). Both measures can be computed by means of the study of vessel tissue deformation along the cardiac cycle.

IntraVascular UltraSound (IVUS) is the best choice to study, both, vessel morphology and its bio-mechanical properties. On one hand, inspection of a single IVUS image gives information about the percentage of stenosis. Manual stenosis measurements require a manual tracing of vessel borders (the internal layer, intima, and the most external one, adventitia). This is a very time-consuming task and might suffer from inter-observer variations. On the other hand, inspection of longitudinal views provides information about artery bio-mechanical properties. The assessment of bio-mechanical properties requires exploring the evolution of vessel walls and structures along the sequence. Dynamics due to heart pumping (among others) introduces a misalignment of sequence frames, preventing any feasible volumetric measurement or 3D reconstruction. In particular heart dynamics produce two types of motion: longitudinal motion along the catheter pullback and in-plane motion of each single cross section. Longitudinal dynamics produces a sequence block with spatially shuffled frames, which hinders any analysis along the sequence. Heart pumping also introduces a periodic rotation and translation in IVUS cross-sections, which hinders proper evaluation of tissue bio-mechanical properties. Both 3D reconstructions and bio-mechanical properties

assessment require a compensation of artery dynamics, either by sampling the sequence synchronized with a cardiac phase or by in-plane sequence stabilization.
Since the early years of IVUS imaging, many algorithms for a reliable intima detection (Bouma et al., 1997; Brathwaite et al., 1996; Brathwaite & McPherson, 1998; Brusseau et al., 2004; Dijkstra et al., 2001; Gil et al., 2000; Hansen et al., 2002; Luo et al., 2003; Mendizabal-Ruiz et al., 2008; Sonka et al., 1996; von Birgelen et al., 1996; 1997) and plaque characterization (de Korte et al., 2000; Escalera et al., 2008; Granada et al., 2007; Nair et al., 2002; Okubo et al., 2008) have been proposed. Most of them are based on the appearance of structures in images. Adventitia modeling has been a delicate issue hardly addressed e.g. (Dijkstra et al., 1999; Gil et al., 2006; Haas et al., 2000; Klingensmith et al., 2000; Olszewski et al., 2004; Plissiti et al., 2004; Pujol & Radeva, 2005; Sonka et al., 1995; Takagi et al., 2000), though it is crucial for stenosis measurement. This is due to its weak appearance in IVUS images, which makes appearance-based techniques fail to produce optimal results and forces ad-hoc elaborated strategies. Also, image-based cardiac phase retrieval strategies are based on image appearance and extract cardiac phase by exploring its temporal changes across the sequence (Barajas et al., 2007; Matsumoto et al., 2008; Nadkarni et al., 2005; Sean M. O'Malley, 2006; Zhu et al., 2003). Speckle, texture and morphology introduce non-cardiac irregular variations in appearance patterns that must be carefully filtered.
So far, dynamics has only been considered as an artifact which is, at most, corrected (Hernàndez-Sabaté et al., 2009; Rosales et al., 2004). We claim that rigid motion estimation is a useful tool for exploring, both, vessel structures and cardiac dynamics. The main concern of this chapter is to show the benefits of cardiac dynamics for adventitia segmentation and image-based cardiac phase retrieval.
The general scheme for adventitia segmentation can be split in three main steps sketched in figure 1.

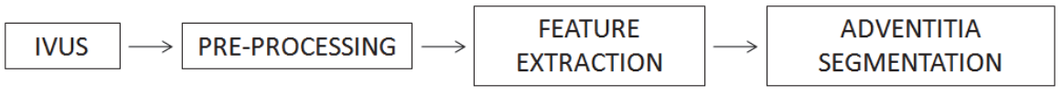

Fig. 1. Pipeline for Adventitia Segmentation

The poor image quality as well as large variety of IVUS artifacts (calcium, side-branches, shadows, catheter guide and blood back scatter) force an elaborated pre-processing step for enhancing adventitia appearance. In order to ensure a good compromise between preservation of the adventitia weak appearance and speckle smoothing, a filtering carefully driven for each image is compulsory (Gil et al., 2006; Unal et al., 2006). This makes the pre-processing stage to be one of the most computationally expensive tasks of the whole scheme. We claim that IVUS (in-plane) rigid motion can significantly improve the smoothing step, since vessel structures follow a periodic motion (induced by heart beat) clearly different from the chaotic random behavior of textured and blood areas. We propose using the mean of stabilized sequence blocks in order to enhance vessel structures while blurring texture and speckle.
Concerning image-based ECG-gating, existing strategies (Barajas et al., 2007; Matsumoto et al., 2008; Nadkarni et al., 2005; Sean M. O'Malley, 2006; Zhu et al., 2003) follow the scheme sketched in figure 2.
First, a signal reflecting cardiac motion is computed from IVUS sequences. Second, the signal is filtered (in the frequency domain) in order to remove non-cardiac phenomena and artifacts. Finally, a suitable sampling of the filtered signal retrieve cardiac phase. All authors agree in

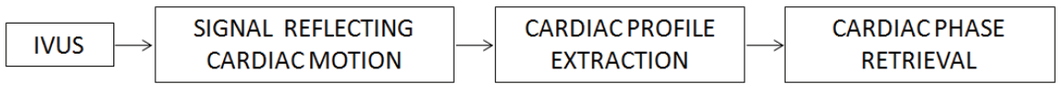

Fig. 2. Pipeline for Image-based Cardiac Phase Retrieval

using a band-pass filter in the second step and the extrema of filtered signals for sampling at end-systole and diastole. The main differences among existing algorithms and thus, the clue for an accurate cardiac phase retrieval, lie in the signal computed from the sequence. Given that in-plane and out-of-plane cardiac motion are coupled, we propose using the periodic component of in-plane motion as the signal reflecting cardiac motion.
In this chapter we propose an integrative framework for retrieving vessel morphology and cardiac phase from IVUS rigid dynamics. Vessel structures extracted from IVUS sequences and stabilized by correcting cardiac dynamics produce stable models of arteries containing deformation along all cardiac cycle and, thus, useful for exploring biomechanics. The collection of vessel structures at frames synchronized at the same fraction of the cardiac cycle provide static models for computing 3D measurements. The pipeline of our integrative framework is sketched in figure 3 where the three clinical tools presented in the chapter are highlighted in orange.

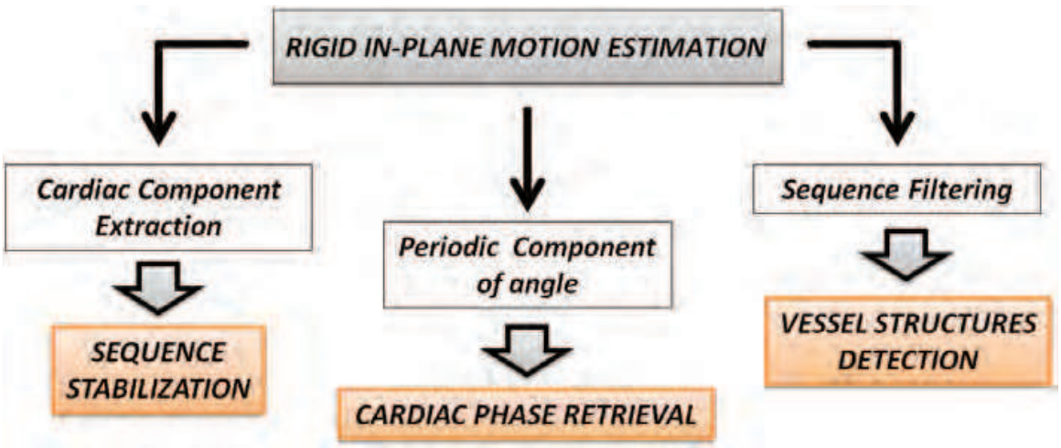

Fig. 3. Pipeline for the Integrative Framework

The remainder of the chapter is structured as follows. In section 2 we sketch the method used to compute rigid in-plane motion (Hernàndez-Sabaté et al., 2009). Section 3 is devoted to detail the three steps which constitute the integrative framework we propose. In section 4 we explain the validation protocol while results are given in section 5. Finally, discussions about the advantages and limitations of using rigid in-plane dynamics compared to appearance methods will be given in the last section of the chapter.

2. Rigid in-plane motion estimation

Different factors such as heart pumping, blood pressure or artery geometric properties mainly contribute to the dynamics of coronary arteries (Holzapfel et al., 2002; Mazumdar, 1992; Nadkarni et al., 2003). The first order approximation to vessel in-plane dynamics is given by a linear transformation combining translation, rotation and scaling (Waks et al., 1996). Dilation is inherent to the elasticity of the vessel itself and it does not preserve the metric. The rigid part of this approximation can be modeled as a rigid body motion and is given by a rotation

followed by a translation. Figure 4 shows the physics-based model of the rigid motion of an artery. The computation of the translation and rotation angle is as follows (Hernàndez-Sabaté et al., 2009).

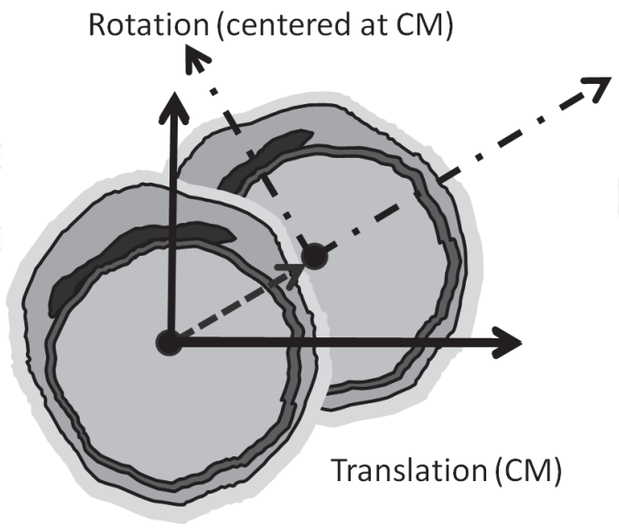

Fig. 4. Physics-based model: rigid solid motion

2.1 Translation

In body dynamics, the point describing the object response to external forces and torques is determined by means of its center of gravity or mass (Goldstein et al., 2002). The difference between its position and the origin of coordinates is identified to the object translation. We note it as VCM which is computed from IVUS frames as follows.

Since grey level reflects tissue mass density due to IVUS images reconstruction, the center of mass given by the image intensity, namely ICM, corresponds to the physical center of gravity of the vessel. However, some acquisition devices allow interactive tuning of the image brightness in order to enhance tissue and vessel structures appearance (Mintz & Nissen, 2001). Given that such intensity gain is radial (Caballero et al., 2006), tissue close to the catheter might look brighter and, for vessels not centered at the catheter, intensity gainings might deviate the position of ICM from the true center of mass. Vessel geometric center, namely GCM, coincides with the vessel center of gravity only in the case of uniform tissue density. However, it serves to compensate the deviation of ICM for non centered vessels. We define the center of mass of the vessel, VCM, by a combination of ICM and GCM achieving a good compromise between vessels whose intensity gain has been tuned and vessels with uniform tissue density.

The center of mass of the image intensities is given by:

$$ICM = \left(\frac{\sum_{i=1}^{n} i \sum_{j=1}^{m} I(i,j)}{\sum_{i=1}^{n} \sum_{j=1}^{m} I(i,j)}, \frac{\sum_{j=1}^{m} j \sum_{i=1}^{n} I(i,j)}{\sum_{i=1}^{n} \sum_{j=1}^{m} I(i,j)} \right)$$

The geometric center of mass of a set of N points roughly lying on the adventitia (the most stable structure along the sequence) (x_k, y_k) is computed as follows:

$$GCM = \frac{1}{N} \left(\sum_{k=1}^{N} x_k, \sum_{k=1}^{N} y_k \right)$$

Finally, the following formula weights both centers of mass, taking into account the deviation of the vessel from the center of the image (Hernàndez-Sabaté et al., 2009):

$$VCM = DR \cdot ICM + (1 - DR) \cdot GCM \tag{1}$$

where DR is the vessel-catheter deviation rate (i.e. the deviation of the vessel from the center of the image). If we consider the maximum, R_{max}, and minimum, R_{min}, distances of the set $(x_k, y_k)_k$ to the image center, DR is defined as:

$$DR = \frac{min_k(\sqrt{x_k^2 + y_k^2})}{max_k(\sqrt{x_k^2 + y_k^2})} = \frac{R_{min}}{R_{max}}$$

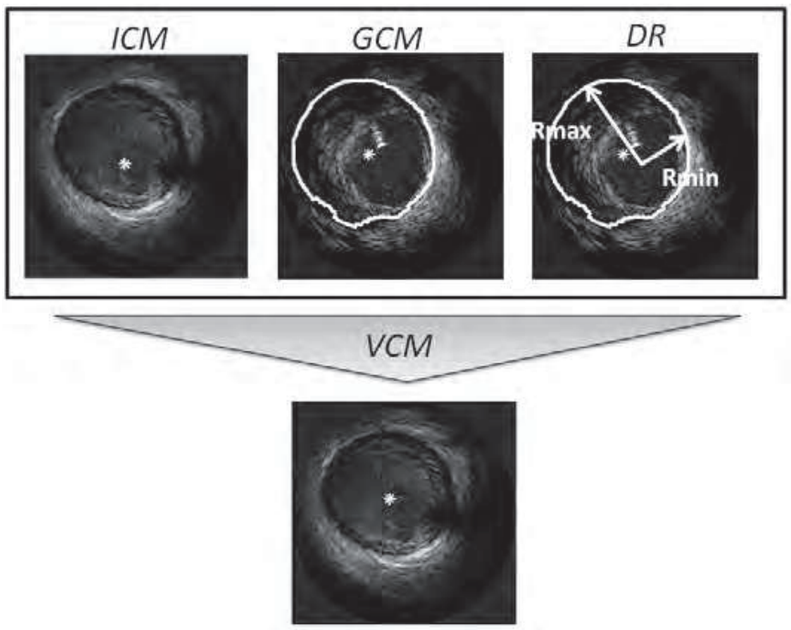

Fig. 5. Computation of the Vessel Center of Mass

We note that in case the artery is centered at the catheter, DR measures its eccentricity. Figure 5 shows the computation of the Vessel Center of Mass from computation of the Image and Geometric Centers of Mass given by formula (1).

2.2 Rotation

Once vessel translation has been compensated, two global motions still remain: rotation and radial scaling. In the polar domain with origin VCM, they convert into a horizontal translation (corresponding to rotation) and a vertical scaling (corresponding to radial scaling). In the case of human coronary arteries, scaling is very close to 1 (Ramírez, 2005), so $\lambda = 1 + \varepsilon$ becomes a perturbation of identity given by ε (Hernàndez-Sabaté, 2009). The horizontal translation is estimated by means of the computation of the phase of the ratio of Fourier transforms of every two consecutive frames (Hernàndez-Sabaté et al., 2009).
That is, if I_1, I_2 are two functions (images) that differ in a pure translation:

$$I_2(i, j) = I_1(i - t_1, j - t_2)$$

the first order approximation to I_2 can be computed by applying the Fourier transform (Oppenheim & Willsky, 1997) and using phase correlation (Kuglin & Hines, 1975). Let $\widehat{I}_1$, $\widehat{I}_2$ be the Fourier transforms of I_1 and I_2, respectively, then they are related via:

$$\widehat{I}_2(\omega) = \widehat{I}_1(\omega) e^{-i\langle \omega, t \rangle}$$

for $\vec{\omega} = (\omega_1, \omega_2)$ the Fourier frequency, $\vec{t} = (t_1, t_2)$ and $\langle \vec{\omega}, \vec{t} \rangle = \omega_1 t_1 + \omega_2 t_2$ the Euclidean scalar product.
If we consider the phase, $\rho(\omega)$, of the ratio between the two Fourier transforms (Alliney, 1993), then we have that:

$$\rho(\omega) = \rho\left(\frac{\widehat{I}_2(\omega)}{\widehat{I}_1(\omega)}\right) = \rho\left(e^{-i\langle \omega, t \rangle}\right) = \langle \omega, t \rangle \ = \omega_1 t_1 + \omega_2 t_2$$

so that the points $(\omega_1, \omega_2, \rho(\omega))$ lie on a plane, Π, with the slopes given by the translation components:

$$\Pi : \rho(\omega) = t_1 \omega_1 + t_2 \omega_2$$

In practice, noise and texture introduce a scatter in the set $(\omega_1, \omega_2, \rho(\omega))$, especially for

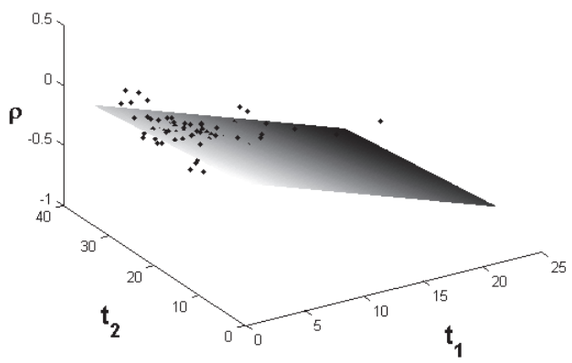

Fig. 6. Regression plane approximating Fourier phase correlation between two shifted images.

those frequencies with smaller amplitudes. We reduce noise-scatter by only considering those frequencies common to both images with an associated amplitude larger than a given percentile. Such frequencies with the phase ρ yield a point cloud, like the one shown in figure 6, which regression plane provides a least-square estimator of the plane Π. The first slope of that regression plane, t_1, estimates the angle of rotation between two consecutive frames.

3. Stable models of arteries

Tissue bio-mechanical properties (like strain and stress) are playing an increasing role in diagnosis and long-term treatment of intravascular coronary diseases. Their assessment strongly relies on estimation of vessel wall deformation along the cardiac cycle. On one hand, image misalignment introduced by vessel-catheter motion is a major artifact for a proper tracking of tissue deformation. On the other hand, longitudinal motion artifacts in IVUS

sequences hinders a properly 3D reconstruction and vessel measurements. Furthermore, vessel plaque assessment by analysis of IntraVascular UltraSound sequences is a useful tool for cardiac disease diagnosis and intervention. Manual detection of luminal (inner) and medial-adventitial (external) vessel borders is the main activity of physicians in the process of lumen narrowing (plaque) quantification. Difficult definition of vessel border descriptors, as well as, shades, artifacts, and blurred signal response due to ultrasound physical properties trouble automated adventitia segmentation.

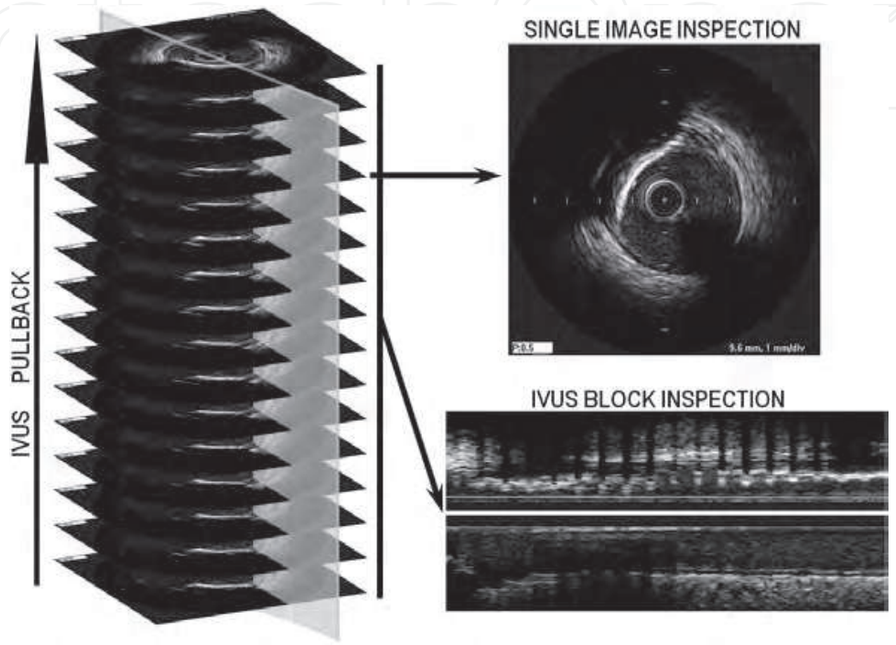

Fig. 7. Images extracted from an IVUS pullback. The left image is a block of 16 IVUS consecutive frames from a constant pullback. The right top image is a single cross-section of the vessel. The right bottom image is a longitudinal view obtained by intersecting 401 frames with the grey plane at the same angle.

Figure 7 shows a block of IVUS images obtained from a pullback (on the left) and the two kind of images derived from them (on the right). Each sequence frame (on the top right) shows a cross-section of the vessel under study with a complete detail of its morphology. The frames on the left can be intersected by a longitudinal plane including the catheter trajectory (grey plane on fig.7, left graphic), defined by a fixed angle on cross sections. The image obtained in this way is called longitudinal cut of the artery (bottom-right image). The image misalignment can be appreciated in the echo-shadowing calcified plaque of the upper profile of the longitudinal cut.

A framework integrating the solution for the three limitations of IVUS (image misalignment, longitudinal motion and adventitia segmentation) should be of utmost importance for clinical practice. In the above section, we have presented a method for assessing IVUS rigid in-plane motion. This estimation allows us to compute the following three steps for achieving an integrative framework of stable models of arteries useful for clinical practice. On one hand, translation and rotation estimation serves to stabilize the sequence by removing cardiac dynamics. On the other side, we present the potential of rigid motion estimation for approaching cardiac phase retrieval from coronary IVUS sequences without ECG signal for

correction of longitudinal motion artifacts. Finally, we show the benefits of using stabilized sequences for improving the computational time of automatic adventitia segmentation algorithms.

3.1 Sequence stabilization

The rigid motion that cardiac vessels undergo is a complex dynamical process which results from the combination of several contributions. In general, it presents a geometric component related to the artery 3D shape and a dynamic one induced by breathing and cardiac movements (Rosales et al., 2004). Depending on the particular problem to approach, each of the terms should have a specific treatment. Exploring artery geometry might be derived by analyzing the geometric component (Rotger et al., 2006), whereas extraction of cardiac dynamics concerns the cardiac dynamical contribution (Zhu et al., 2003). In the case of vessel biomechanics analysis, the goal is to produce a static model allowing a better tissue tracking along the segment. Firstly, the reader should note that, without further analysis, the geometric component does not reach a reliable 3D representation of the vessel geometry, which might lead to wrong static models. Secondly, even if one could infer the true 3D geometry from it, by compensating vessel tortuosity there is no guarantee of a better alignment of vessel plaque. This suggests only correcting the dynamical terms of the translation and rotation for stabilizing the sequence.

For that, the signal obtained is decoupled in the Fourier domain into geometric, breathing and cardiac component and the last component serves to stabilize the images along the sequence (Hernàndez-Sabaté, 2009). The translation and rotation parameters are functions of the time s. If the geometric term of a motion parameter is denoted by the subindex $_g$, the cardiac term, induced by heart beating, is denoted by the subindex $_c$ and breathing contributions are denoted by the subindex $_b$, the angle and translation decompose into:

$$\begin{aligned} t(s) &= t_g(s) + t_b(s) + t_c(s) \\ \theta(s) &= \theta_g(s) + \theta_b(s) + \theta_c(s) \end{aligned} \tag{2}$$

Focusing on the Fourier series of these components, breathing and cardiac terms are periodic and, thus, have a discrete Fourier spectrum, whereas geometry has a broad-band (non-discrete) spectrum (Oppenheim & Willsky, 1997). As usual, Fourier transforms are indicated by a hat ($\hat{}$) over functions. Principal harmonics have been learned by supervised classification of the spectrum of a training set of 30 patients without apparent lesions used in a study for assessment of myocardial perfusion in contrast angiography (Gil et al., 2008). Confidence intervals of the 95% yield the expected ranges for the principal frequency of each of the periodic components. For breathing it is $(10, 45)$ repetitions per minute (rpm), while for cardiac motion it is $(45, 200)$ rpm. Thus, cardiac motion principal harmonic, ω_c, is defined as the first local maximum in $I_{\omega_c} = (45, 200)$ rpm and the term is approximated by the first 10 harmonics, $(k\omega_c)_{k=1:10}$. For the sake of an efficient algorithm, ω_c is approximated by the global maximum of Fourier transform amplitude for frequencies in the range $I\omega_c$. It follows that the cardiac motion term of a sequence lasting N_{Sec} seconds is given by:

$$t_c(s) = \frac{1}{T}\sum_{k=1}^{k=10} \widehat{t}(k\omega_c)e^{ik\omega_c s} \quad \theta_c(s) = \frac{1}{T}\sum_{k=1}^{k=10} \widehat{\theta}(k\omega_c)e^{ik\omega_c s}$$

where the period $T = N_{Sec}/60$ is the sequence length (in minutes) and defines the domain of integration.

Since, even in healthy cases, the heart rate varies along the pullback, the peaks in the Fourier series are spread around the theoretic harmonic frequencies. The more irregularities in periodicity are, the more spread around the theoretic harmonic the Fourier development is. The harmonics less corrupted by noise are obtained by optical filtering (Klug & D.J.DeRosier, 1966). Optical filtering is a technique widely used in electron crystallography in order to discard harmonics corrupted with noise. Optical filtering selects only those harmonics presenting a prominent peak. The peakedness of an harmonic is given by the normalized difference between the amplitude achieved at the harmonic and an average of amplitudes in a neighborhood $I_{k\omega_c}$ centered at the harmonic:

$$OF(k\omega_c) = \frac{|F(k\omega_c)|}{S} - \frac{1}{N \times S} \sum_{x \in I_{k\omega_c} \setminus k\omega_c} |F(x)| \tag{3}$$

where F stands for either t or θ, $S = \sum_{x \in I_{k\omega_c}} |F(x)|$ and N is the number of harmonics in $I_{k\omega_c}$. Harmonics selected by optical filtering are the only contributions to the sums in (3).

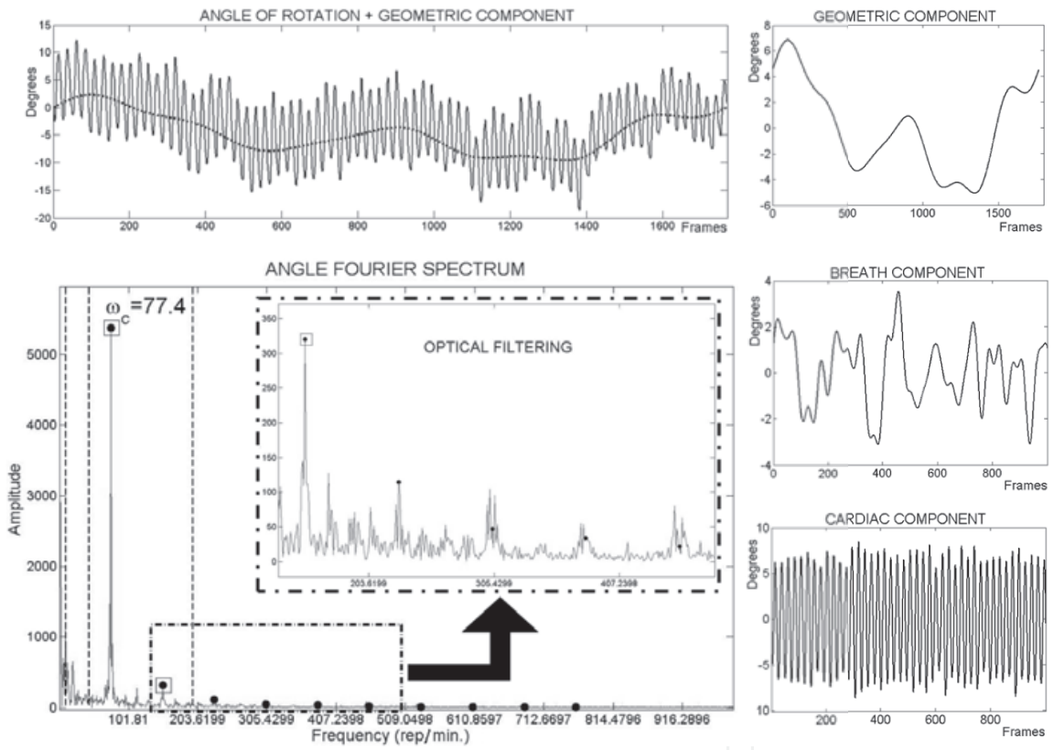

Fig. 8. Motion Decomposition. Rotation angle and its Fourier decomposition on the left; geometric, breathing and cardiac terms on the right.

Figure 8 shows the Fourier terms decoupling for the rotation angle in the top left plot. Vertical lines in the Fourier spectrum of the signal (bottom left plot) indicate the ranges defined for the 3 phenomena. Dots mark the 10 cardiac harmonics and squares the ones selected after optical filtering. The 3 components of the angle are shown in right plots.
Finally, the linear application mapping the artery at a given time to the artery at time zero is given by:

$$\begin{pmatrix} \tilde{x} \\ \tilde{y} \end{pmatrix} = \begin{pmatrix} \cos(\theta_c) & -\sin(\theta_c) \\ \sin(\theta_c) & \cos(\theta_c) \end{pmatrix} \begin{pmatrix} x - VCM_c^x \\ y - VCM_c^y \end{pmatrix} \tag{4}$$

for $VCM_c = (VCM_c^x, VCM_c^y)$ the cardiac component of the position of the vessel center of mass and θ_c the cardiac component of the angle of rotation in degrees.

3.2 Cardiac phase retrieval

The first step for modeling longitudinal motion in IVUS sequences is retrieving information about the cardiac phase. Following the general scheme shown in figure 9, our image-based algorithm to approach ECG sampling (Hernàndez-Sabaté et al., 2011) splits in the following three steps.

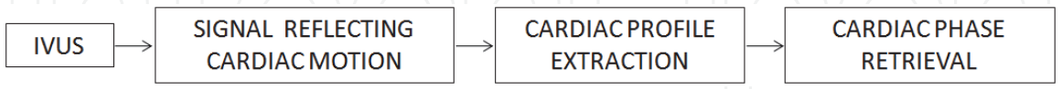

Fig. 9. Pipeline for Image-based Cardiac Phase Retrieval

1. **Extraction of Signal Reflecting Cardiac Motion:**
   By the physical coupling (Nadkarni et al., 2003), luminal area evolution is synchronized to other vessel cardiac phenomena, such as tissue motion or rigid motion. It follows that, since rigid in-plane motion comes from artery motion due to heart pumping, the angle of rotation is also synchronized to cardiac phase. In particular the periodic component, θ_c, given in Section 2 is a signal reflecting (pure) cardiac motion.
2. **Signal Filtering for Cardiac Profile Extraction:** Even in healthy subjects, cardiac frequency does not remain constant along the sequence. This artifact introduces (among other phenomena) irregularities in the Fourier transform of the cardiac motion profile. The irregularities distort the cardiac signal and corrupt the location of local extrema in the signal reflecting cardiac motion. Following the literature, we filter the cardiac profile with two families of band-pass filters centered at the cardiac frequency ω_c: Butterworth (B) (Zhu et al., 2003) and Gaussian-based (g) (Matsumoto et al., 2008).
   The Butterworth filter is defined as:

$$B(\omega) = \frac{1}{\sqrt{1 + \left(\frac{|\omega| - \omega_c}{0.6\Delta\omega_c}\right)^{2n}}}$$

   where n is related to the filter decay and $\Delta\omega = \delta\omega_c$ to its support. Meanwhile, the Gaussian filter is defined as:

$$g(\omega, \sigma) = \frac{1}{\sigma\sqrt{2\pi}} e^{-(|\omega| - \omega_c)^2/(2\sigma^2)}$$

   In this case, the decay cannot be handled (it is always exponential) and only its support might be tuned by its deviation σ.
   Figure 10 shows a signal reflecting cardiac motion filtered by a Butterworth filter with parameters $n = 2, \delta = 0.1$. In the top left image, we present the original filter. The Fourier transform is computed and shown in the bottom left image. The result of the product between its Fourier transform and the filter is shown in the bottom right image. The final result is shown in the top right image.
   The real part of the inverse Fourier transform of the filtered cardiac profile is a smooth signal suitable for cardiac phase retrieval. Regardless of the filter used we will denote it by $Filt$.

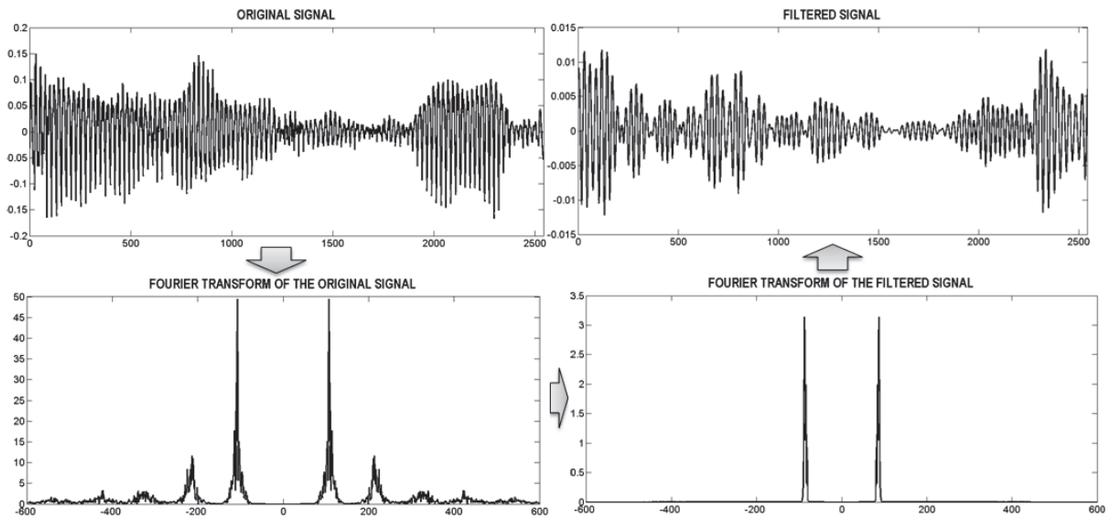

Fig. 10. Signal filtering with a Butterworth filter with parameters $n = 2; \delta = 0.1$

Figure 11 plots the rotation motion profile on a longitudinal cut (on the left) and the profile filtered on the same cut (on the right). Note that the most prominent minimums and maximums of the cardiac profile, on the left, correspond to the minimums and maximums of the filtered signal on the right, though it is necessary to filter the signal in order to extract the cardiac phase.

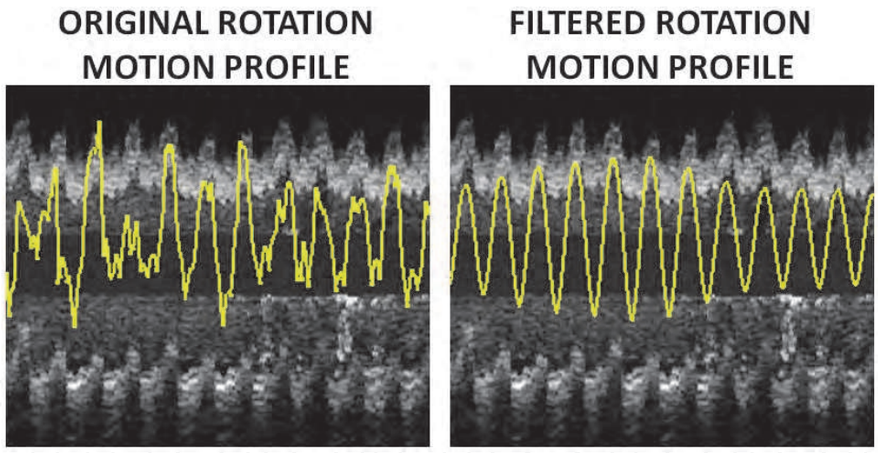

Fig. 11. Original rotation motion profile and the corresponding filtered one.

3. **Cardiac Phase Retrieval:** Maximums and minimums of the filtered signal give a sampling at end-systole and end-diastole and, thus, retrieve cardiac phase for each selected pixel. Extrema positions are computed in the Fourier domain using the equation:

$$\widehat{f'} = 2\pi i\omega \hat{f}$$

for speeding up the process, since $\hat{f}$ has already been computed.

3.3 Vessel structures detection

The strategy for media-adventitia (simply adventitia from now on) segmentation we suggest follows the general scheme presented in (Gil et al., 2006) summarized in figure 12. First, a pre-processing step simplifies the appearance of adventitia, as well as, enhances significant structures while removing noise and textured tissue. Second, the feature extraction task computes two different masks and, by combining them, we obtain those points that most probably correspond to the adventitia layer. Finally, a closing stage delineates the adventitia layer.

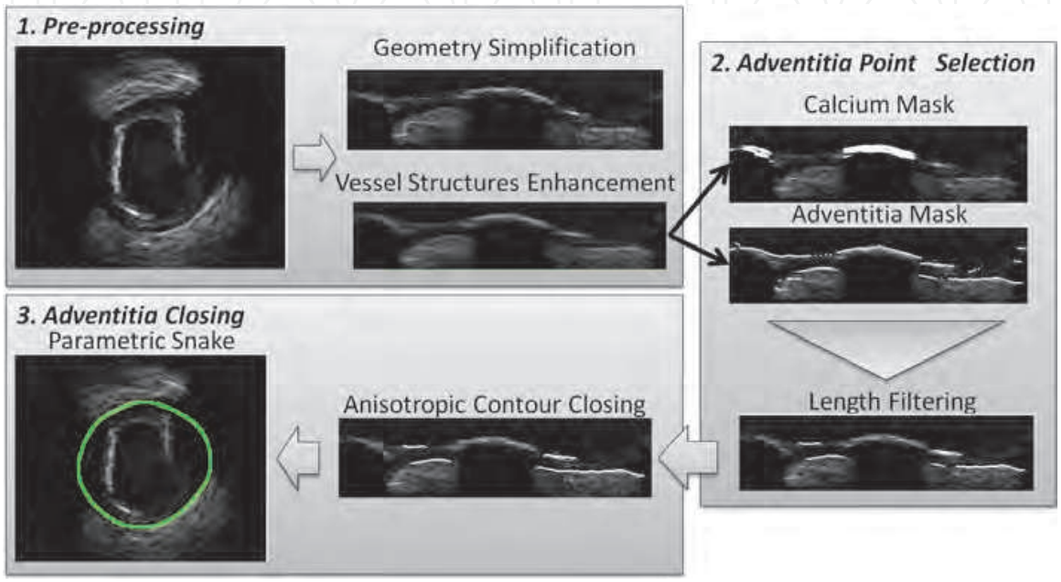

Fig. 12. Adventitia Detection Flow (Gil et al., 2006)

In the pre-processing step, in order to enhance significant structures while removing noise and textured tissue, some kind of filtering is necessary. The most extended way of preserving adventitia thin structure (Gil et al., 2006; Takagi et al., 2000) is by using anisotropic filtering, like the Structure Preserving Diffusion (SPD) introduced in (Gil et al., 2010). Given that such diffusions are computed by means of iterative schemes, the filtering step is, generally, the most time consuming task of the algorithm. For instance, the SPD filtering used in (Gil et al., 2006) takes about the half of the total time and it can consume up to 1.54 seconds per frame.
We observe that, after rigid motion compensation, image pixel intensity, which is related to tissue density of mass, remains more uniform along frames. It follows that the mean of stabilized sequence blocks enhances vessel structures, while blurring texture and speckle. We propose replacing the SPD by the mean of stabilized sequences, namely MSS. The remaining steps of the process are the same reported in (Gil et al., 2006). Figure 13 shows the same image given in the general scheme of fig. 12 filtered using SPD diffusion and MSS. For a better comparison across filters, we show images in cartesian (top) and polar (bottom) domains.

4. Validation protocol

4.1 Sequence stabilization

The quality of sequence stabilization exclusively relies on the accuracy of the estimated parameters of rigid in-plane motion. Given that their accuracy has been assessed

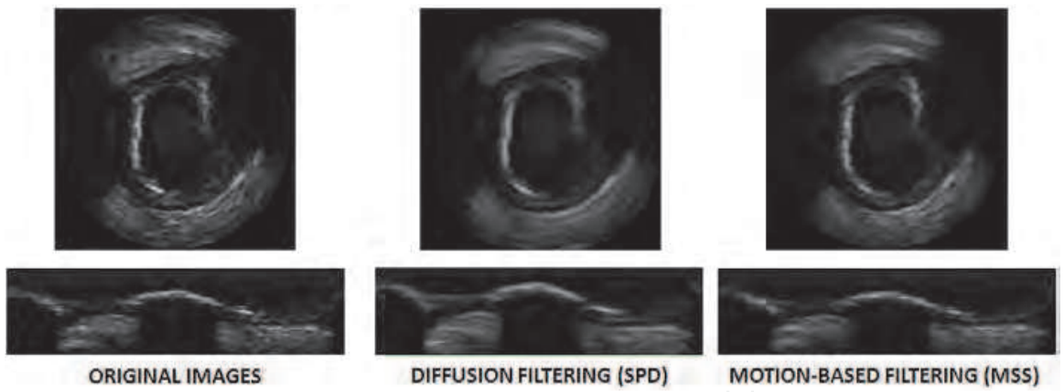

Fig. 13. Enhancement of vessel structures by using a diffusion filter (center images) and the mean of stabilized sequences (left images).

in (Hernàndez-Sabaté et al., 2009), we prefer only to visually illustrate the quality of stabilizations. Cardiac motion introduces a misalignment in IVUS images, as well as, irregular profiles in longitudinal cuts. Therefore, the quality of stabilizations will be visually checked by longitudinal cuts obtained from original sequences and after sequence stabilization.

4.2 Cardiac phase retrieval

For the assessment of cardiac phase retrieval, we have compared the automatic phase retrieval to a manual sampling of the sequence. Automatic samplings were compared to the frames achieving extrema lumen areas. These extrema were manually detected by exploring longitudinal cuts by selecting minimums and maximums of intima/lumen and media-adventitia transition profiles. The distances between each manual detected frame and the automatic one most close to it were computed. That is, if s^k and $\tilde{s}^k$ are frame positions in the sequence for a manual and automatic sampling respectively, we define their distance as the absolute differences between their positions:

$$E^k = |s^k - \tilde{s}^k|$$

The distances of all frames provide a distance map for each patient. As for in-plane dynamics, we retrieve a single quantity for each sequence (seq) by averaging E^k over all sampled frames (N):

$$E^1_{seq} = \frac{1}{N}\sum_{k=1}^{N} E^k$$

Statistical ranges (given by the mean $\pm$ the variance, $\mu \pm \sigma$) of errors for all patients indicate the accuracy of each of the method.

In order to detect if there are any significant differences among smoothing filters (that is, a best/worst performer), we have used the multiple comparison methodology (Nemenyi test) proposed in (Demsar, 2006). For each sequence (trial) the M filters (there are 12 in our case and might be considered as classifiers) are ranked according to their errors. The ranking assigns 1 to the best performer and M for the worst one. The average ranks are statistically compared to find out if there are any significant differences. The significance level for computing and comparing ranks in the Nemenyi test is 0.1.

Finally, we have checked the benefits of using dynamic quantities by comparing results to the ones obtained using gray-intensity cardiac signals (Hernàndez-Sabaté et al., 2011).

Therefore for the sake of a faithful comparison, the experimental set is the same used in (Hernàndez-Sabaté et al., 2011): 22 vessel segments 420-690 frames long (7-11.5 mm approximately) recorded with a Galaxy-BostonSci device at 40 MHz, with a rotating single transducer and constant pullback speed of 0.5 mm./s. The digitalization rate was 30 fps.

4.3 Vessel structures detection

The goal of this experiment is checking wether the rotation angle can produce accurate enough adventitia segmentations, while significantly reducing computational time. Therefore, we have compared segmentations obtained using MSS filtering to SPD diffusion (Gil et al., 2006) in terms of quality of the segmentations and computational cost.
In this case, ground truth is given by manual identification of the adventitia in IVUS images. Since discrepancies among experts provide a non-unique ground truth, we follow the same protocol described in (Gil et al., 2006), based on comparisons of inter-observer variability to manual segmentations. The accuracy has been assessed by means of absolute (in millimeters) and relative (in percent) distances. If $p = (x_p, y_p)$ denotes the points corresponding to an automatic contour, its absolute distance to the manual contour is defined as:

$$D(p) = min_{q \in \gamma} \sqrt{(x_p - x_q)^2 + (y_p - y_q)^2} \tag{5}$$

and relative distances correspond to the ratio:

$$RelD(p) = 100 \cdot \frac{D(p)}{d(q, O)}$$

for the origin O the center of mass of the manual contour and q the point achieving the minimum in (5). Absolute distances are given in mm and relative ones in percentages.
For each distance error, we compute its maximum and mean values on the automated contour to measure accuracy in positions.

- Maximum distance errors:

$$MaxD = max_p(D(p) \cdot PixSze))$$
$$RelMaxD = max_p(RelD(p))$$

- Mean distance errors:

$$MeanD = mean_p(D(p) \cdot PixSze))$$
$$RelMeanD = mean_p(RelD(p))$$

for PixSze denoting the image spatial resolution and p is any point on the automatically traced adventitia. The interval given by the mean $\pm$ standard deviation computed over the 4 experts contours indicate the statistical range of values for each of the automated errors (MaxD, RelMaxD, MeanD, RelMeanD). Inter-observer variability is obtained by computing the error measures for the models made every two independent observers and it, thus, quantifies discrepancy among experts.
Concerning computational time, we have considered maximums and ranges for the following tasks: Rigid In-plane Motion Estimation (RME), adventitia segmentation by means of Mean of Stabilized Sequences (MSS), adventitia segmentation by means of Structures Preserving Diffusion (SPD). For a better quantification of time improvement, we have also considered

the ratio between both segmentation techniques (SPD/MSS) and the ratio taking into account the time computation for Rigid In-plane Motion Estimation (SPD/(MSS+RME)).
Since we want to compare MSS filtering to the anisotropic filtering used in (Gil et al., 2006), the experimental setting is the same reported in (Gil et al., 2006). A total number of 5400 images extracted from 22 vessel segments of a length ranging from 4 to 6 mm (200-300 frames). Sequences were recorded with a Boston Scientific Clear View Ultra scanner at 40 MHz with constant pull-back at 0.5 mm/s and a digitalization rate of 25 frames/s.

5. Results

5.1 Sequence stabilization

Figure 14 shows two longitudinal cuts taken at the white lines on the IVUS left image and the same cut after sequence alignment. Each IVUS image cuts present the two main artifacts induced by vessel dynamics in *in vivo* pullbacks. The upper longitudinal cuts show the saw-tooth-shape pattern of the vessel intima wall (dark line) introduced by relative vessel-catheter translation. The profile of bottom cuts presents a structure misalignment due to the relative vessel-catheter rotation for an echo-shadowing calcified plaque. After sequence stabilization, the vessel wall profiles of upper cuts are straight and continuous, whereas calcium shows a uniform appearance.

5.2 Cardiac phase retrieval

As in (Hernàndez-Sabaté et al., 2011), the set of filters scanned, G_i for gaussian filters and B_i for Butterworth ones is the following.

$$G_1 : \{\sigma = 0.001\};\ G_2 : \{\sigma = 1.5\};\ G_3 : \{\sigma = 10\}$$

$$B_1 : \{n = 1, \delta = 0.5\};\ B_2 : \{n = 1, \delta = 0.05\};\ B_3 : \{n = 1, \delta = 0.005\};$$
$$B_4 : \{n = 2, \delta = 0.5\};\ B_5 : \{n = 2, \delta = 0.05\};\ B_6 : \{n = 2, \delta = 0.005\};$$
$$B_7 : \{n = 4, \delta = 0.5\};\ B_8 : \{n = 4, \delta = 0.05\};\ B_9 : \{n = 4, \delta = 0.005\}$$

As well, we have added the results of the angle output without filtering. Two Nemenyi tests have been performed, one (labeled TN_1) to detect differences across filters and another one (labeled TN_2) to compare the impact of the filtering with the angle itself. The first one only includes errors for B_i and G_i, while the second one incorporates the errors obtained by the angle θ_c. Tables 1 and 2, report the average ranks (the smaller, the better) reflecting each filter performance (table 1) and its comparison to the sampling obtained without filtering (table 2).

Filter Param.	G_1	G_2	G_3	B_1	B_2	B_3	B_4	B_5	B_6	B_7	B_8	B_9
Rank	8.12	5.53	6.15	5.71	5.24	7.47	6.06	5.44	7.94	5.56	6.68	8.12

Table 1. TN_1: Average rank of the filters set performance

Filter Param.	G_1	G_2	G_3	B_1	B_2	B_3	B_4	B_5	B_6	B_7	B_8	B_9	θ
Rank	8.29	5.65	6.27	5.82	5.35	7.59	6.18	5.56	8.06	5.68	6.79	8.29	11.47

Table 2. TN_2: Comparison of performance between the filters set and the sampling without filtering

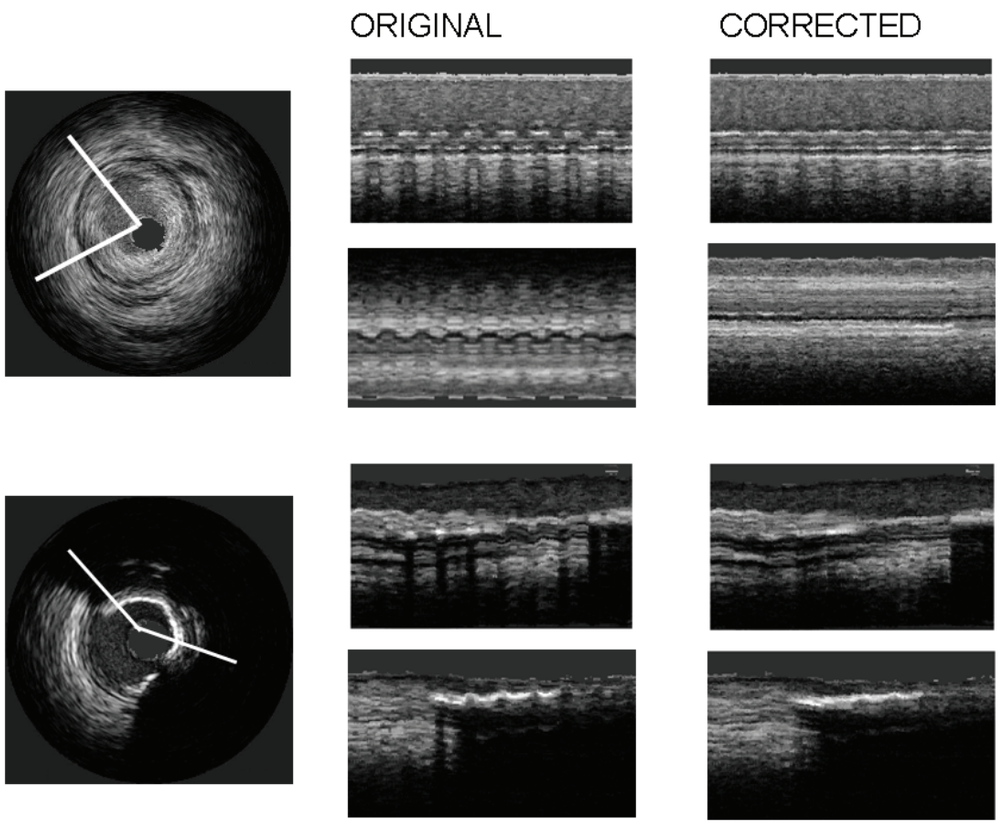

Fig. 14. Longitudinal cuts for sequences of two patients. The first column corresponds to a representative original frame, for each patient, with the angle of the longitudinal cuts. In the second column, the original longitudinal cut and the corrected one in the third column.

The Nemenyi critical difference (CD) for TN_1 is 3.75, while for TN_2 is 4.11. The test detects that the sampling without filtering is significatively worst than the filtered ones. However, the Nemenyi test also reports that there is not enough evidence of a significantly different performance among the filtered methods.
Figures 15 and 16 show the rank of samplings from left to right (the best is on the left) together with the critical difference in order to visually compare them. In figure 15 we can note that there is no significative difference among the filters. However, in figure 16, we can appreciate that the sampling without filtering is clearly separated from the rest.

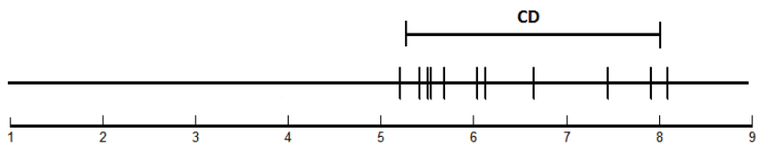

Fig. 15. Visually comparison of different filters using NT_1.

Table 3 reports the ranges, by the mean $\pm$ the variance ($\mu \pm \sigma$) of the 8 filters of the set with better ranks. Values in the first column are in frames, the ones of the second column are in seconds and the last column correspond to the values in millimeters. As figure 15 shows,

Fig. 16. Visually comparison of different filters to the sampling without filtering using NT_2.

there is no significative difference between them. The Butterworth filter with $n = 1$ and $\delta = 0.05$ achieves the best results with an error within 3.55 ± 1.80 frames, which corresponds to 0.06 ± 0.03 mm.

Method	Frames	Seconds	Millimeters
G_2	3.5601 ± 1.9804	0.1187 ± 0.0660	0.0593 ± 0.0330
G_3	3.6974 ± 1.8520	0.1232 ± 0.0617	0.0616 ± 0.0309
B_1	3.6416 ± 1.8747	0.1214 ± 0.0625	0.0607 ± 0.0312
B_2	3.5498 ± 1.7998	0.1183 ± 0.0600	0.0592 ± 0.0300
B_4	3.6824 ± 1.8478	0.1227 ± 0.0616	0.0614 ± 0.0308
B_5	3.7468 ± 1.5738	0.1249 ± 0.0525	0.0624 ± 0.0262
B_7	3.6660 ± 1.8423	0.1222 ± 0.0614	0.0611 ± 0.0307
B_8	4.0192 ± 1.6035	0.1340 ± 0.0534	0.0670 ± 0.0267

Table 3. Average Errors of the best set of filters

In order to compare the ranges of the approach proposed in this chapter to the ones presented in (Hernàndez-Sabaté et al., 2011) table 4 reports the ranges of the filters presented in table 3 in frames (1st column), seconds (2nd column) and millimeters (3rd column). We can observe that there is no significative difference as a Nemenyi test proves.

Method	Frames	Seconds	Millimeters
G_1	3.8644 ± 1.7497	0.1288 ± 0.0583	0.0644 ± 0.0292
G_2	3.8929 ± 1.6648	0.1298 ± 0.0555	0.0649 ± 0.0277
B_1	4.0240 ± 1.6105	0.1341 ± 0.0537	0.0671 ± 0.0268
B_2	$\mathbf{3.8972 \pm 1.8001}$	0.1299 ± 0.0600	0.0650 ± 0.0300
B_3	4.4488 ± 1.9458	0.1483 ± 0.0649	0.0741 ± 0.0324
B_4	3.8570 ± 1.7338	0.1286 ± 0.0578	0.0643 ± 0.0289
B_5	4.1506 ± 1.8597	0.1384 ± 0.0620	0.0692 ± 0.0310
B_7	3.8680 ± 1.7279	0.1289 ± 0.0576	0.0645 ± 0.0288
B_8	4.2071 ± 1.8385	0.1402 ± 0.0613	0.0701 ± 0.0306

Table 4. Average Errors of the best set of filters for the image-grey level evolution approach

Figure 17 shows the performance of our method for the Butterworth filtering in 4 large longitudinal cuts. The original cuts are in the left, while the cuts sampled at end diastole rate are in the right. For the first segment, we can notice the continuous profile for the lumen contour, while in the second and third segments, we can follow up the calcium plaques present in the vessel. In the four segment we can appreciate the continuous profile of two bifurcations at the upper side of the cut.

5.3 Vessel structures detection

Table 5 reports the inter-observer variability (INT-OBS) to ranges of automatic errors for SPD and MSS computed for all segments. The results for the MSS algorithm are slightly worse

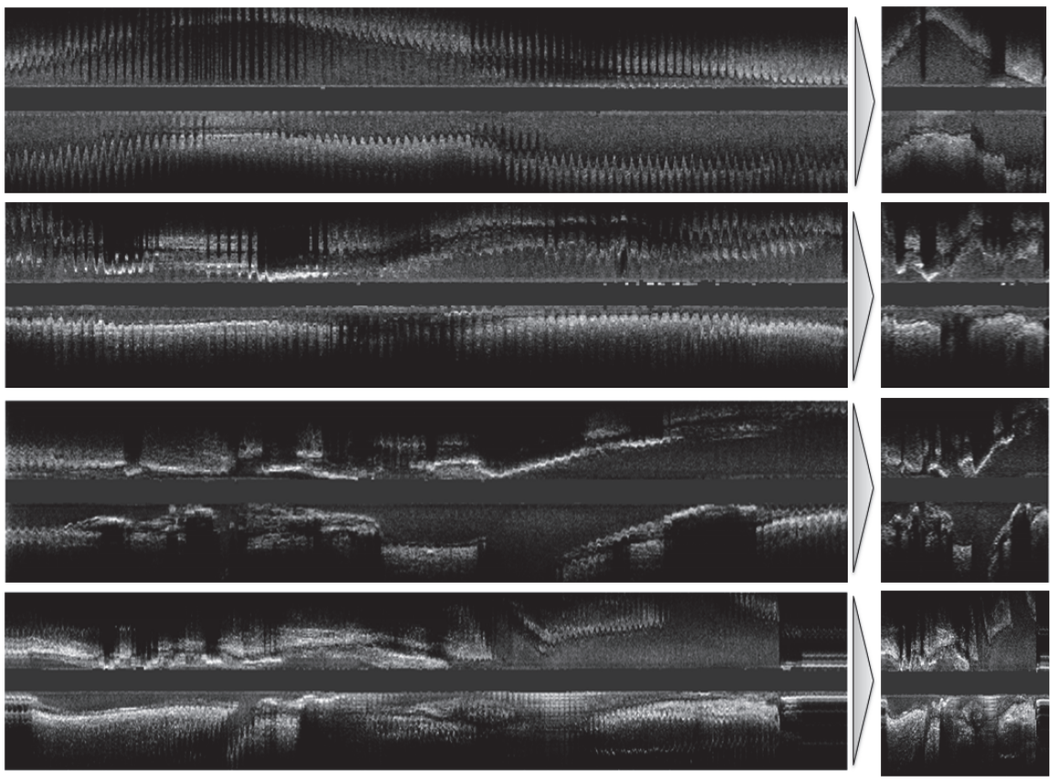

Fig. 17. Results of Image-based ECG sampling for two different longitudinal cuts.

than the ones from the SPD approach. However, note that they are still in the range of inter-observer variability.

	INT-OBS	SPD	MSS
MaxD (mm)	0.5386 ± 0.3075	0.5715 ± 0.2296	0.5988 ± 0.2047
RelMaxD (%)	0.4697 ± 0.2664	0.5122 ± 0.2344	0.5369 ± 0.1953
MeanD (mm)	0.2206 ± 0.1126	0.2265 ± 0.0688	0.2604 ± 0.0879
RelMeanD (%)	0.1888 ± 0.0945	0.1972 ± 0.0662	0.2387 ± 0.0808

Table 5. Performance Evaluation of the Adventitia Segmentation Strategies

Table 6 reports the computational times required for each task: Rigid In-plane Motion Estimation (RME), adventitia segmentation by means of Mean of Stabilized Sequences (MSS), adventitia segmentation by means of Structures Preserving Diffusion (SPD), the ratio between both segmentation techniques (SPD/MSS) and the ratio taking into account the time computation for Rigid In-plane Motion Estimation (SPD/(MSS+RME)). We can observe that the new approach proposed is almost 27 times faster (in average) than the vessel appearance

	RME	MSS	SPD	SPD/MSS	SPD/(MSS+RME)
Max	0.5412	0.0909	2.4379	32.2131	5.5228
Mean	0.3575 ± 0.0673	0.0797 ± 0.0057	2.1282 ± 0.1279	26.8792 ± 2.9042	4.9484 ± 0.6193

Table 6. Times comparison of Adventitia Segmentation Strategies for each frame (in sec.)

diffusion approach. Although rigid in-plane motion estimation is useful for the whole integrative framework, we could take into account the time needed for computing it. Still, the new approach is 5 times faster (in average).

6. Discussions and conclusions

In this chapter we proposed an integrative framework for exploring vessel dynamics and structures, so that to obtain stable models of arteries. We showed the potential of vessel in-plane rigid dynamics to analyze and correct vessel in-plane rigid dynamics, retrieve cardiac phase and aid the automatic segmentation of adventitia layer.
In (Hernàndez-Sabaté et al., 2009) we already proved that rigid in-plane dynamics estimation contributes in a proper image misalignment correction. In this chapter we also showed the usefulness of this estimation for retrieving cardiac phase and we compared the method proposed to other vessel appearance-based models. There are two main advantages in using a dynamic quantity instead of the usual signals computed from image grey-level evolution (Barajas et al., 2007; Hernàndez-Sabaté et al., 2011; Matsumoto et al., 2008; Nadkarni et al., 2005). Firstly, since θ_c does not include non-cardiac phenomena (such as breathing) it requires less specific tuning of the band-pass filtering. Secondly, it is computationally faster. Although errors ranges seem to be worse for the new approach, a Nemenyi test reports that there is no significative differences. Concerning the usefulness of rigid dynamics for the contribution to the adventitia segmentation, the main improvement is the computational time. Nevertheless, the accuracy errors still keep within the range of inter-observer variability.
For that reasons, we can conclude that rigid in-plane dynamics estimation has a high potential for developing useful techniques for clinical practice, and reducing drastically the time computation, since they can be parallelizable.

7. References

Alliney, S. (1993). Spatial registration of multiespectral and multitemporal digital imagery using fast-fourier transform techniques, *IEEE PAMI* 15(5): 499–504.

Barajas, J., Caballero, K., Rodriguez, O. & Radeva, P. (2007). Cardiac phase extraction in IVUS sequences using 1-D gabor filters, *29th Annual International Conference of the IEEE EMBS*.

Bouma, C. J., Niessen, W. J., Zuiderveld, K. J., Gussenhoven, E. J. & Viergever, M. A. (1997). Automated lumen definition from 30 MHz intravascular ultrasound images, *Med. Image Anal* 1: 363–377.

Brathwaite, P., Chandran, K., McPherson, D. & Dove, E. (1996). Lumen detection in human IVUS images using region-growing, *Computers in Cardiology*, pp. 37–40.

Brathwaite, P. & McPherson, K. C. D. (1998). 3D IVUS border detection in highly diseased arteries with dissecting flaps, *Comp. in Card.*, pp. 157–160.

Brusseau, E., de Korte, C., Mastik, F., Schaar, J. & van der Steen, A. F. W. (2004). Fully automatic luminal contour segmentation in intracoronary ultrasound imaging: A statistical approach, *IEEE Trans. Med. Imag* 23(5).

Caballero, K., Barajas, J., Pujol, O., Salvatella, N. & Radeva, P. (2006). In-vivo IVUS tissue classification: A comparison between RF signal analysis and reconstructed images, *Progress in Pattern Recognition, Image Analysis and Applications*, Vol. 4225, pp. 137–146.

Céspedes, E., Korte, C. & van der Steen, A. (2000). Intraluminal ultrasonic palpation: assessment of local cross-sectional tissue stiffness, *Ultrasound Med. Biol.* 26: 385–396.

de Korte, C. L., Pasterkamp, G., van der Steen, A. F. W., Woutman, H. A. & Bom, N. (2000). Characterization of plaque components with intravascular ultrasound elastography in human femoral and coronary arteries in vitro, *Circulation* 102: 617–623.

Demsar, J. (2006). Statistical comparisons of classifiers over multiple data sets, *Journal of Machine Learning Research* 7: 1–30.

Dijkstra, J., Koning, G. & Reiber, J. (1999). Quantitative measurements in IVUS images, *Inter. Journal of Cardiovas. Imag.* 15(6): 513–522.

Dijkstra, J., Koning, G., Tuinenburg, J., Oemrawsingh, P. & Reiber, J. (2001). Automatic border detection in intravascular ultrasound images for quantitative measurements of the vessel, lumen and stent parameters, *Computer Assisted Radiology and Surgery - CARS 2001*, pp. 916–922.

Escalera, S., Pujol, O., Mauri, J. & Radeva, P. (2008). IVUS tissue characterization with sub-class error-correcting output codes, *Computer Vision and Pattern Recognition Workshops, 2008*, pp. 1–8.

Fuster, V. (1994). Mechanisms leading to myocardial infarction: Insights from studies of vascular biology, *Circulation* 90(4): 2126–2146.

Gil, D., Hernàndez, A., Rodriguez, O., Mauri, J. & Radeva, P. (2006). Statistical strategy for anisotropic adventitia modelling in IVUS, *IEEE Transactions on Medical Imaging* 25(6): 768–778.

Gil, D., Radeva, P. & Saludes, J. (2000). Segmentation of artery wall in coronary IVUS images: a probabilistic approach, *Intern. Conf. Pat. Recog.*, pp. 352–355.

Gil, D., Rodriguez-Leor, O., Radeva, P. & Mauri, J. (2008). Myocardial perfusion characterization from contrast angiography spectral distribution, *IEEE Trans. on Med. Imag.* 27(5): 641–649.

Gil, D., Hernàndez-Sabaté, A., Brunat, M., Jansen, S. & Martínez-Vilalta, J. (2010). Structure-preserving Smoothing of Biomedical Images, *Pattern Recognition* 44(9): 1842-1851.

Goldstein, H., Poole, C. & Safko, J. (2002). *Classical Mechanics*, 3rd edn, Addison Wesley.

Granada, J. F., Wallace-Bradley, D., Win, H. K., Alviar, C. L., Builes, A., Lev, E. I., Barrios, R., Schulz, D. G., Raizner, A. E. & Kaluza, G. L. (2007). In vivo plaque characterization using intravascular ultrasound virtual histology in a porcine model of complex coronary lesions, *Arteriosclerosis, Thrombosis, and Vascular Biology* 27: 387–393.

Haas, C., Ermert, H., Holt, S., Grewe, P., Machraoui, A. & Barmeyer, J. (2000). Segmentation of 3D intravascular ultrasonic images based on a random field model, *Ultrasound Med. Biol.* 26(2): 297–306.

Hansen, M., Møller, J. & Tøgersen, F. (2002). Bayesian contour detection in a time series of ultrasound images through dynamic deformable template models, *Biostatistics* 3(2): 213–228.

Hernàndez-Sabaté, A. (2009). *Exploring Arterial Dynamics and Structures in IntraVascular UltraSound Sequences*, PhD thesis, Universitat Autònoma de Barcelona.

Hernàndez-Sabaté, A., Gil, D., Fernandez-Nofrerias, E., Radeva, P. & Martí, E. (2009). Approaching rigid artery dynamics in IVUS, *IEEE Trans. Med. Imag.* 28(11): 1670–1680.

Hernàndez-Sabaté, A., Gil, D., Garcia-Barnés, J. & Martí, E. (2011). Image-based cardiac phase retrieval in intravascular ultrasound sequences, *IEEE Transaction on Ultrasonics, Ferroelectrics, and Frequency Control* 58(1): 60–72.

Holzapfel, G., Gasser, T. & Stadler, M. (2002). A structural model for the viscoelastic behavior of arterial walls: continuum formulation and finite element analysis, *Eur. J. Mech. A-Solids* 23: 1–162.

Kakadiaris, I., O'Malley, S., Vavuranakis, M., Carlier, S., Metcalfe, R., Hartley, C., Falk, E. & Naghavi, M. (2006). Signal-processing approaches to risk assessment in coronary artery disease, *IEEE Signal Processing Magazine* 23(6): 59–62.

Klingensmith, J., Shekhar, R. & Vince, D. (2000). Evaluation of three-dimensional segmentation algorithms for the identification of luminal and medial-adventitial borders in intravascular ultrasound, *IEEE Med. Imag.* 19(10): 996–1011.

Klug, A. & D.J.DeRosier (1966). Optical filtering of electron micrographs: reconstruction of one-sided images, *Nature* 212: 29–32.

Kuglin, C. & Hines, D. (1975). The phase correlation image alignment method, *Int. Conf. on Cybernetics and Society*, pp. 163–165.

Luo, Z., Wang, Y. & Wang, W. (2003). Estimating coronary artery lumen area with optimization-based contour detection, *IEEE Transactions on Medical Imaging* 22(4): 564–566.

Matsumoto, M. M. S., Lemos, P. A., Yoneyama, T. & Furuie, S. S. (2008). Cardiac phase detection in intravascular ultrasound images, *Medical Imaging 2008: Ultrasonic Imaging and Signal Processing*.

Mazumdar, J. (1992). *Biofluids Mechanics*, World Scientific Publishing.

Mendizabal-Ruiz, G., Rivera, M. & Kakadiaris, I. (2008). A probabilistic segmentation method for the identification of luminal borders in intravascular ultrasound images, *IEEE Conference on Computer Vision and Pattern Recognition. CVPR 2008.*, pp. 1–8.

Mintz, G. & Nissen, S. (2001). Clinical expert consensus document on standards for acquisition, measurement and reporting of intravascular ultrasound studies (IVUS), *JACC* 37(5): 1478–92.

Nadkarni, S. ., Boughner, D. . & Fenster, A. . (2005). Image-based cardiac gating for three-dimensional intravascular ultrasound imaging, *Ultrasound in Medicine and Biology* 31(1): 53–63.

Nadkarni, S., Austin, H. & et al (2003). A pulsating coronary vessel phantom for two and three-dimensional intravascular ultrasound studies., *Ultrasound Med. Biol.* 29(4): 621–628.

Nair, A., Kuban, B. D., Tuzcu, E. M., Schoenhagen, P., Nissen, S. E. & Vince, D. G. (2002). Coronary plaque classification with intravascular ultrasound radiofrequency data analysis, *Circulation* 106: 2200–2206.

Okubo, M., Kawasaki, M., Ishihara, Y., Takeyama, U. et al. (2008). Tissue characterization of coronary plaques: comparison of integrated backscatter intravascular ultrasound with virtual histology intravascular ultrasound, *Circulation* 72(10): 1631–9.

Olszewski, M. E., Wahle, A., Mitchell, S. C. & Sonka, M. (2004). Segmentation of intravascular ultrasound images: a machine learning approach mimicking human vision, *CARS*, pp. 1045–1049.

Oppenheim, A. & Willsky, A. (1997). *Signals and Systems*, 2n edn, Prentice-Hall.

Plissiti, M., Fotiadis, D., Michalis, L. & Bozios, G. (2004). An automated method for lumen and media-adventitia border detection in a sequence of IVUS frames, *IEEE Infor. Tech. Biomed.* 8(2): 131–141.

Pujol, O. & Radeva, P. (2005). *Handbook of Medical Image Analysis: Advanced Segmentation and Registration Models*, Kluwer Academic/ Plenum Publishers, chapter Supervised Texture Classification for Intravascular Tissue Characterization, pp. 57–110.

Ramírez, M. D. R. (2005). *A Physics-Based Image Modelling of IVUS as a Geometric and Kinematics System*, PhD thesis, Universitat Autònoma de Barcelona.

Rosales, M., Radeva, P., Mauri, J. & Pujol, O. (2004). Simulation model of intravascular ultrasound images, *MICCAI*, Vol. 3217, pp. 200–7.

Rotger, D., Radeva, P. & Rodriguez, O. (2006). Vessel tortuosity extraction from IVUS images, *Comp. in Card.*, pp. 689–692.

Sean M. O'Malley, Morteza Naghavi, I. A. K. (2006). Image-based frame gating for contrast-enhanced IVUS sequences, *International Workshop on Computer Vision for Intravascular and Intracardiac Imaging, International Workshop on CVIII, MICCAI*.

Sonka, M., Zhang, X., DeJong, S. C., Collins, S. M. & McKay, C. R. (1996). Automated detection of coronary wall and plaque borders in ECG-gated intravascular ultrasound pullback sequences (abstract), *Circulation* 94 (Suppl.).

Sonka, M., Zhang, X. & Siebes, M. (1995). Segmentation of intravascular ultrasound images: A knowledge based approach, *IEEE Med. Imag.* 14: 719–732.

Takagi, A., Hibi, K., Zhang, X., Teo, T. J., Bonneau, H. N., Yock, P. G. & Fitzgerald, P. J. (2000). Automated contour detection for high-frequency IVUS imaging: a technique with blood noise reduction for edge enhancement, *Ultrasound Med. Biol.* 26(6): 1033–1041.

Unal, G., Bucher, S., Carlier, S., Slabaugh, G., Fang, T. & Tanaka, K. (2006). Shape-driven segmentation of intravascular ultrasound images, *Proc. of the International Workshop on Computer Vision for Intravascular Imaging (CVII), MICCAI*, pp. 50–57.

von Birgelen, C., Mario, C., Li, W., Schuurbiers, J., Slager, C., de Feyter, P., Roelandt, J. & Serruys, P. (1996). Morphometric analysis in three-dimensional intracoronary ultrasound: An in vitro and in vivo study performed with a novel system for the contour detection of lumen and plaque, *Am. Heart Journal* 132: 516–527.

von Birgelen, C., Mintz, G. S., Nicosia, A., Foley, D. P., van der Giessen, W. J., Bruining, N., Airiian, S. G., Roelandt, J. R. T. C., de Feyter, P. J. & Serruys, P. W. (1997). Electrocardiogram-gated intravascular ultrasound image acquisition after coronary stent deployment facilitates on-line three-dimensional reconstruction and automated lumen quantification, *J. Amer. Coll. Cardiol.* 30: 436–443.

Waks, E., Prince, J. & Andrew, S. (1996). Cardiac motion simulator for tagged MRI, *Proceeding of MMBIA. IEEE.*

Wentzel, J., Krams, R., Schuurbiers, J. H., Oomen, J., Kloet, J., van der Giessen, W., Serruys, P. & Slager, C. (2001). Relationship between neointimal thickness and shear stress after wallstent implantation in human coronary arteries, *Circulation* 103(13): 1740–5.

Zhu, H., Oakeson, K. D. & Friedman, M. H. (2003). Retrieval of cardiac phase from IVUS sequences, *Medical Imaging 2003: Ultrasonic Imaging and Signal Processing*, Vol. 5035, pp. 135–146.

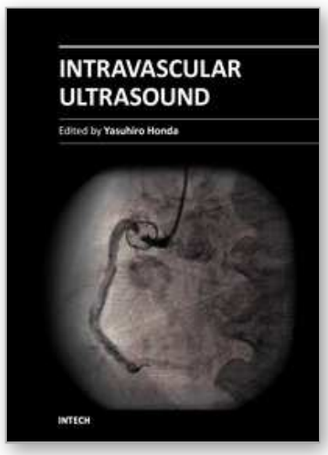

Intravascular Ultrasound
Edited by Dr. Yasuhiro Honda

ISBN 978-953-307-900-4
Hard cover, 207 pages
Publisher InTech
Published online 01, February, 2012
Published in print edition February, 2012

Intravascular ultrasound (IVUS) is a cardiovascular imaging technology using a specially designed catheter with a miniaturized ultrasound probe for the assessment of vascular anatomy with detailed visualization of arterial layers. Over the past two decades, this technology has developed into an indispensable tool for research and clinical practice in cardiovascular medicine, offering the opportunity to gather diagnostic information about the process of atherosclerosis in vivo, and to directly observe the effects of various interventions on the plaque and arterial wall. This book aims to give a comprehensive overview of this rapidly evolving technique from basic principles and instrumentation to research and clinical applications with future perspectives.

InTech Europe
University Campus STeP Ri
Slavka Krautzeka 83/A
51000 Rijeka, Croatia
Phone: +385 (51) 770 447
Fax: +385 (51) 686 166
www.intechopen.com

InTech China
Unit 405, Office Block, Hotel Equatorial Shanghai
No.65, Yan An Road (West), Shanghai, 200040, China
中国上海市延安西路65号上海国际贵都大饭店办公楼405单元
Phone: +86-21-62489820
Fax: +86-21-62489821

IntechOpen